Nonlinear ground-state pump-probe spectroscopy in an ultracold rubidium system

Arthur K. Mills[1] and D. S. Elliott[1,2]
[1]*School of Electrical and Computer Engineering, Purdue University, West Lafayette, Indiana 47907, USA*
[2]*Department of Physics, Purdue University, West Lafayette, Indiana 47907, USA*
(Received 24 August 2012; published 17 December 2012)

We present results of our experimental investigations of nonlinear ground-state pump-probe spectroscopy in ultracold ^{85}Rb collected in a magneto-optical trap. These measurements represent an extension of a similar pump-probe spectroscopy in a two-level atomic system when strongly driven by a near-resonant pump beam. In the present three-level system, coherence-induced gain at the probe laser frequency can be observed at specific frequencies within the spectrum. The absorption or gain spectra that we observe resemble those of the two-level gain spectra, but different interference processes lead to features that are not present in the two-level case. We describe our measurements of this interaction in this work.

DOI: 10.1103/PhysRevA.86.063819 PACS number(s): 42.62.Fi, 42.65.Dr, 42.50.Gy

I. INTRODUCTION

A two-level atomic system driven by a coherent, single-frequency, near-resonant laser (pump) field is known to exhibit sideband structure, with the energy spacing between these sidebands determined by the Rabi frequency of the interaction [1]. A weak probe field, nearly degenerate with the pump field, exhibits a distinctive absorption or gain spectrum when interacting with this system, showing features when resonant with transitions between states of the dressed atom [2]. The gain observed in this system is based upon an atomic coherence produced in the atom by the pump beam rather than an inversion of the bare state population of the system. Pump-probe spectroscopy in strongly driven two-level systems has been explored extensively both theoretically [3–6] and experimentally [7–11].

Coherence effects in atomic three-level systems have proven to be an even richer arena. Λ-configuration three-level systems, when the terminal states are components of the ground state, can be long lived since the ground states do not decay, allowing for entangled states in these systems [12–14]. Normally absorbing atomic vapors can be made transparent through electromagnetically induced transparency (EIT) [15–17], and slowing and storage of light [18] has been demonstrated. Recently, subwavelength localization of excited atomic states through coherent population trapping has been investigated [19–21].

With recent availability of high-power tunable laser sources, Raman-coupling strengths can be quite large, even when the detuning of the laser frequencies from the intermediate state resonance is large, permitting superposition states with significant amplitude in each ground-state component, but with little or no population of the intermediate state. Thus, measurements of the probe beam absorption or gain spectrum in a Raman-coupled ground-state atom become interesting as a means of fully exploring the behavior of this highly nonlinear system.

Berman and Dubetsky [22] considered the system shown in Fig. 1 theoretically. While the spectra that they calculated are similar in some regards to those of the two-level system [2], they also discovered a new interference effect that leads to different features in the spectrum. In the present work, we explore this nonlinear ground-state pump-probe spectroscopy in a system of ultracold atomic ^{85}Rb and report our observations of absorption and gain features in these spectra. The hyperfine structure of ^{85}Rb presents technical challenges to observing the system under the conditions assumed by Berman and Dubetsky that we discuss in the next section, which includes significant effects due to spontaneous emission and optical pumping. To study these effects we record transient probe absorption in order to observe the evolution of the probe absorption in real time as optical pumping processes take place. While conditions assumed in the theory could not be fully attained in the laboratory, many of the qualitative features predicted by Berman and Dubetsky in the steady state are apparent in our spectra.

In this work, we observe gain and absorption in a weak probe laser interacting with a three-level atomic system driven by a pair of strong laser fields that couple the two ground states of the Λ system. We observe direct signatures of the two-photon Rabi frequency through the probe absorption, as measured on the real-time probe beam intensity. The spectra of the transmitted probe beam show prominent features at the sideband frequencies of the driven system, as predicted by Berman and Dubetsky. In the following, we discuss the underlying theory, describe our experimental configuration, and present our results.

II. THEORY

Berman and Dubetsky [22] proposed a type of nonlinear ground-state pump-probe (NLPP) spectroscopy for probing the ground-state structure of an atomic medium dressed by a strong Raman interaction. The specific interaction involves three coherent laser fields interacting with a three-level atomic medium in a Λ configuration, as shown in Fig. 1.

The levels labeled $|1\rangle$ and $|2\rangle$ can be, for example, two hyperfine levels of the atomic ground state, while the level $|e\rangle$ is an excited state that is dipole-coupled to both states $|1\rangle$ and $|2\rangle$ through the two pump fields E_1 and E_2, respectively. The field frequencies of the probe field E and the pump fields E_1 and E_2 are described by Ω, Ω_1, and Ω_2, respectively, and the detunings of the fields from their respective transition frequencies are given by

$$\Delta = \Omega - \omega_{e1}, \quad \Delta_1 = \Omega_1 - \omega_{e1}, \quad \Delta_2 = \Omega_2 - \omega_{e2}, \qquad (1)$$

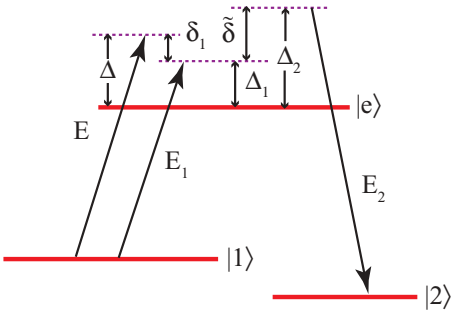

FIG. 1. (Color online) Three-level atomic system driven by two pump fields E_1 and E_2, and probed by a field E.

where ω_{ei} is the atomic transition resonance frequency between states $|e\rangle$ and $|i\rangle$. Following the notation of Ref. [22], the single-photon Rabi frequencies for the $|i\rangle \rightarrow |e\rangle$ transitions are $2\chi_i = \mu_{\mathbf{i}} \cdot \mathbf{E_i}/\hbar$. The relative magnitude of χ_1 and χ_2 is characterized by $\eta = \sqrt{\chi_1/\chi_2}$. In our measurements, described in the following section, states $|1\rangle$, $|2\rangle$, and $|e\rangle$ are served by the $5s\ ^2S_{1/2}, F = 3$, $5s\ ^2S_{1/2}, F = 2$, and $5p\ ^2P_{3/2}$ states of atomic ^{85}Rb, respectively. Two-photon Rabi frequencies and Stark shifts are of key importance in this experiment. Specifically, the two-photon Rabi frequencies are defined as

$$g = \chi_1\chi_2/\Delta, \quad g' = \chi\chi_2/\Delta, \tag{2}$$

where g describes the coupling between states $|1\rangle$ and $|2\rangle$ by pump fields E_1 and E_2, and g' describes the coupling due to pump E_2 and the probe E. While g' is much smaller than g, it is not negligible in the theory. The Stark shifts are defined as

$$S_1 = \chi_1^2/\Delta, \quad S_2 = \chi_2^2/\Delta, \quad S = \chi\chi_1/\Delta. \tag{3}$$

The detunings Δ_1 and Δ_2 are chosen to be large enough that the population of $|e\rangle$ remains small, yet small enough to yield a large two-photon Rabi frequency, g. Two key detunings are the pump-probe detuning δ_1 and the two-photon detuning $\tilde{\delta}$, which are defined as

$$\delta_1 = \Delta - \Delta_1 = \Omega - \Omega_1, \tag{4}$$

$$\tilde{\delta} = \Delta_2 - \Delta_1 = \Omega_2 - \Omega_1 + \omega_{21}, \tag{5}$$

where ω_{21} is the hyperfine splitting of the ground state (for our choice of states, $\omega_{21} = \omega_2 - \omega_1$ is negative).

The two-photon detuning of these pump fields from the Raman transition, $\tilde{\delta}$, is small, leading to strong Raman coupling of states $|1\rangle$ and $|2\rangle$. The effective, Stark-shifted two-photon detuning is given by

$$\delta = \tilde{\delta} - (S_1 - S_2). \tag{6}$$

In analogy with the dressed states of a two-level atom, the ground states in this interaction can be considered as being dressed by the two-photon pump field, as detailed in Ref. [22]. The frequency separation of the dressed states is given by

$$\omega_{BA} = \sqrt{\delta^2 + 4g^2}, \tag{7}$$

where the dressed states $|A\rangle$ and $|B\rangle$ are superpositions of the bare states $|1\rangle$ and $|2\rangle$, and the form of ω_{BA} is reminiscent of the generalized Rabi frequency in a two-level system.

Berman and Dubetsky calculated the absorption spectrum of a probe field E, detuned from the $|1\rangle \rightarrow |e\rangle$ transition by Δ

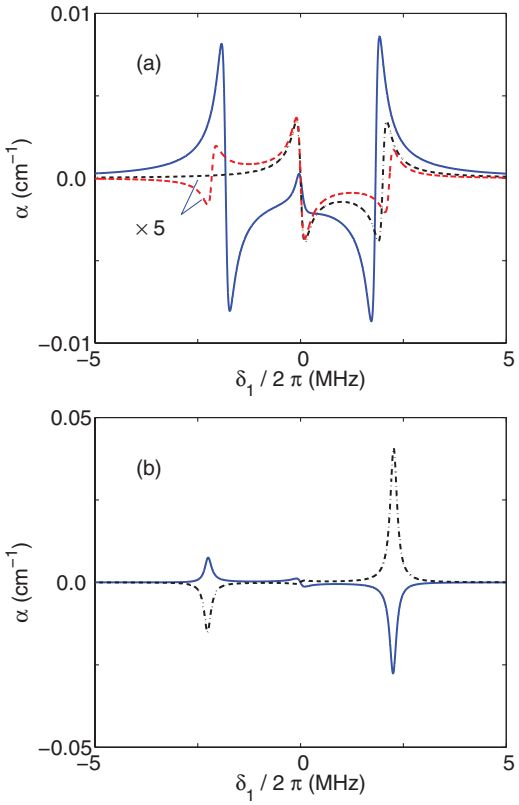

FIG. 2. (Color online) Absorption spectra of the probe beam. (a) The Stark-shift-corrected two-photon detuning δ of E_1 and E_2 is set to 0, while the relative amplitudes of the two laser fields are characterized by $\eta = 1/5$ (solid line, blue), $\eta = 1$ (dot-dashed line, black), or $\eta = 5$ (dashed line, red). (b) We vary the detuning from two-photon resonance, keeping $\eta = 2$ in each trace. The solid line shows the absorption spectrum for $\delta = -g$, while in the dot-dashed curve $\delta = g$.

as a function of $\delta_1 \equiv \Delta - \Delta_1$. We show a few of their spectra in Fig. 2.

In Fig. 2(a), we show examples of probe absorption spectra for $\delta = 0$ for three different pump beam intensity ratios ($\eta = 1/5$, 1, and 5). For each, $\Gamma/2\pi = 0.1$ MHz is the loss rate of the ground state, as described in Ref. [22], and the two-photon Rabi frequency is $g = 10\Gamma$, or $g/2\pi = 1$ MHz. Since ground states are by definition very long lived, losses are due primarily to atoms expanding out of the interaction region. On these curves, $\alpha < 0$ indicates gain. For $\eta = 1/5$ (weak E_1), shown as the solid blue curve, the absorption consists of three dispersion-shaped line shapes, centered near $\delta_1 = -\omega_{BA} = -2g$, 0, and $\omega_{BA} = 2g$. The central feature at $\delta_1 = 0$ is relatively small compared to those at $\delta_1 = \pm 2g$. For $\eta = 1$ (χ_1 and χ_2 are equal), shown as the dot-dashed black curve, the magnitude of the central feature is comparable to that at $\delta_1 = 2g$, while the peak at $\delta_1 = -2g$ has vanished. Finally, when $\eta = 5$ (weak E_2), shown as the red dashed curve, the peak at $\delta_1 = -2g$ has reappeared, but it is inverted relative to its appearance for weak E_1, and the magnitudes of the three peaks are comparable with one another. Note that we have magnified the curves for $\eta = 1$ and 5 by a factor of 5 to improve their visibility. The variation in the ratio of the beam intensities I_1 and I_2 for the two pump beams is extremely large ($\sim 4 \times 10^5$) between $\eta = 1/5$ and

$\eta = 5$, much larger than one can realistically attain in the laboratory. Still, these plots illustrate the wide variability of the probe absorption spectra with pump beam intensities.

In Fig. 2(b), we show the probe absorption spectra for two different two-photon detunings, $\delta = -g$ for the solid blue curve, and $\delta = +g$ for the black dot-dashed curve. We keep $\eta = 2$ for each case. The resonances at $\delta_1 = \pm\omega_{BA} = \pm\sqrt{5}g$ are no longer dispersion shaped, but rather single-peaked absorption or gain. The peak at $\delta_1 = +\sqrt{5}g$ dominates: a gain peak for $\delta = -g$, but an absorption peak for $\delta = +g$. The feature at $\delta_1 = -\sqrt{5}g$ is of the opposite sign from the primary peak and the dispersion-shaped resonance at $\delta_1 = 0$ is small in each case. The central peak shows an interesting property as one varies η. For $\eta > 1.5$, this peak inverts as we switch the detuning from $\delta = -g$ to $\delta = +g$. At $\eta \sim 1.5$, however, this peak vanishes, and for $\eta < 1.5$, the peak remains the same from $\delta = -g$ to $\delta = +g$.

In addition to the analysis based on the time dependence of the amplitudes of the eigenstates of the three-level atom interacting with the three laser fields, Berman and Dubetsky also developed a dressed-state analysis of the interaction. This picture allows simple interpretation of the gain and absorption peaks in terms of the admixture coefficients of the dressed states, as well as their equilibrium population. Absorption results when a probe photon is scattered into one of the pump fields, associated with an atomic transition among the dressed states. Gain is observed in the probe when the transition moves in the opposite direction, scattering a pump photon into the probe field. As we describe in the next section, we have used a cooled and trapped atomic ^{85}Rb system to carry out the measurements of probe gain and absorption.

III. EXPERIMENT

We investigate the NLPP process in an ultracold sample of approximately 1×10^8 ^{85}Rb atoms produced in a magneto-optical trap (MOT). Suppression of Doppler broadening, as in the trapped atoms, is important in these measurements in order to maintain uniform detunings, Δ_1, Δ_2, and Δ, for all atoms. The experiment is cycled between loading and probe cycles, in which the MOT beams and the magnetic field are switched off and the NLPP experimental fields are switched on to probe the freely expanding cloud of atoms.

After preparation in the MOT, the Rb atoms are left in the $F = 3$ hyperfine level of the ground $5s\,^2S_{1/2}$ state. This state serves as state $|1\rangle$ of the three-level system. We couple this initial state to the $F = 2$ hyperfine level of the ground state, level $|2\rangle$, via a two-photon Raman interaction driven by two intense pump fields E_1 and E_2, whose generation we describe later in this section. The frequencies of the pump fields are close to resonance with the $5p\,^2P_{3/2}$ state, which serves as level $|e\rangle$. We show the relevant energy levels of ^{85}Rb, including hyperfine structure of the $5s\,^2S_{1/2}$ and $5p\,^2P_{3/2}$ states, in Fig. 3. We have chosen the polarizations of the lasers to be linear and perpendicular to one another to optimize the Raman coupling strength at large detunings. Defining the quantization axis of the atoms parallel to the field of E_2, this field couples hyperfine components of the same m_F, shown as the solid lines in Fig. 3. E_1 couples components whose z component of F differs by

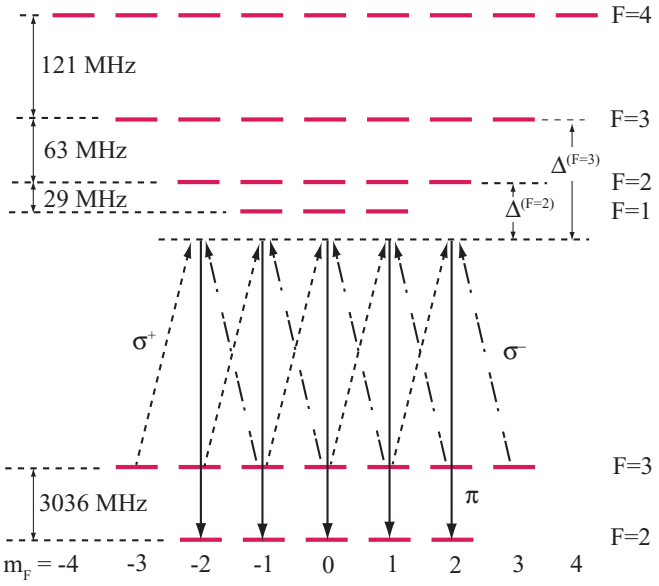

FIG. 3. (Color online) Energy-level schematic of the D_2 line of ^{85}Rb including two-photon pump laser excitation with lin ⊥ lin excitation. For the frequency of the lasers shown here, Δ is negative.

$\Delta m_F = \pm 1$, labeled as dashed (σ^+) and dot-dashed (σ^-) lines in Fig. 3.

For each of our measurements, it is instructive to calculate the relevant Rabi frequencies of the interactions and Stark shifts of the levels. We determine the Rabi frequencies χ_1 and χ_2 of the one-photon interactions for each of the transitions indicated in Fig. 3, for all hyperfine levels F of the $5p\,^2P_{3/2}$ state, using the known transition moment and Clebsch-Gordon coefficients [23]. Due to the selection rule $\Delta F = 0$ or ± 1 for single-photon electric dipole transitions, only the $F = 2$ and $F = 3$ levels of the $5p\,^2P_{3/2}$ state contribute to the Raman coupling of levels $|1\rangle$ and $|2\rangle$. To determine the two-photon Rabi frequency g for the $5s\,^2S_{1/2}$, $F = 3$, $m_F \rightarrow 5s\,^2S_{1/2}$, $F = 2$, $m_F \pm 1$ transition given by Eq. (2), we evaluate $\chi_1\chi_2/\Delta$ for each of these two intermediate states, and add. For transitions starting from the extreme components $|m_F| = 3$, we find

$$|g^{(|m_F|=3)}|/2\pi = \left| \frac{0.279}{\Delta^{(F=3)}/2\pi} + \frac{0.559}{\Delta^{(F=2)}/2\pi} \right| \sqrt{I_1 I_2}, \quad (8)$$

where $\Delta^{(F=3)}$ and $\Delta^{(F=2)}$ represent the detuning from the $F = 3$ and $F = 2$ excited states, the frequencies $g^{(i)}/2\pi$ and $\Delta^{(i)}/2\pi$ are given in megahertz, and the pump intensities I_1 and I_2 are given in W cm^{-2}. Only one Raman transition ($\Delta m_F = -1$ for $m_F = 3$ and $\Delta m_F = +1$ for $m_F = -3$) is active for these components. For two-photon transitions starting from $|m_F| = 2$, we find

$$|g^{(|m_F|=2)}|/2\pi = \left| \frac{0.456}{\Delta^{(F=3)}/2\pi} + \frac{0.228}{\Delta^{(F=2)}/2\pi} \right| \sqrt{I_1 I_2} \quad (9)$$

for the stronger allowed transitions (i.e., $\Delta m_F = -1$ for $m_F = 2$ and $\Delta m_F = +1$ for $m_F = -2$). As we show later, our measurements suggest that these are the dominant transitions involved in the NLPP process. For determination of the Stark shifts S_1 and S_2, we use Eq. (3). For S_1, we calculate χ_1^2/Δ

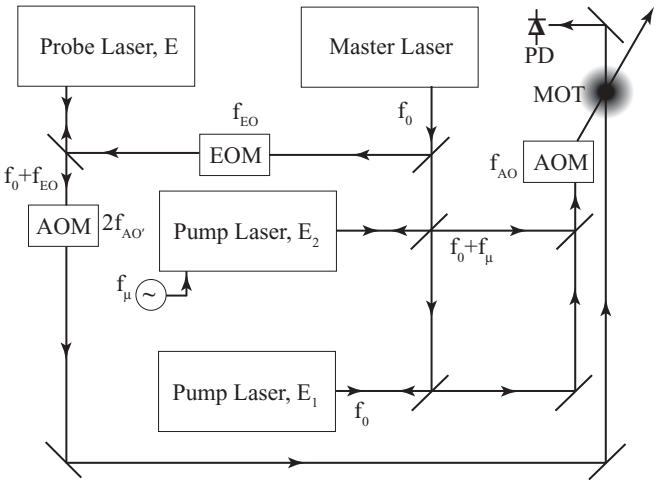

FIG. 4. Simplified experimental setup illustrating the arrangement used to derive the pump fields, E_1 and E_2, and the probe field, E, from a single master laser. The pump fields are combined on a polarizing beam splitter, switched with an AOM, and directed into the MOT. The transmission of the probe beam through the MOT is continuously monitored by a fast photodetector (PD).

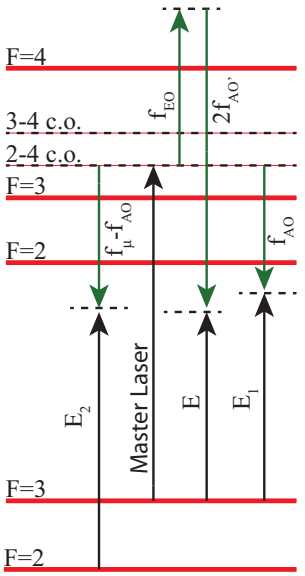

FIG. 5. (Color online) Illustration showing the derivation of the frequencies involved in the experiment relative to the resonant frequencies from the ^{85}Rb $F = 3$ ground state to the $F = 2$, 3, and 4 excited states ($F = 1$ excited state not shown). The laser frequencies are shown in black, and the frequency modulation offsets are shown as green arrows. The frequency Ω_0 of the master laser is stabilized to a saturated absorption crossover resonance (designated '2–4 c.o.' in the figure). Laser E_1 is derived from the master laser with an AOM frequency shift, f_{AO}. The probe laser E is derived with a frequency shift from an EOM (f_{EO}) and a double-pass AOM shift ($2 \times f_{\mathrm{AO}'}$). Laser E_2 is derived from the master laser with a microwave frequency offset, and an AOM frequency shift, f_{AO}.

for each of the dipole-allowed levels ($F = 2$, 3, and 4) of the $5p\,^2P_{3/2}$ state, and sum. Similarly, for S_2, we sum χ_2^2/Δ over the $F = 1$, 2, and 3 levels of the $5p$ state. The Stark shifts are relatively insensitive to m_F of the initial state, as expected.

To carry out the NLPP measurements, we require two pump beams of amplitudes E_1 and E_2, each at a relatively high intensity, and a weak probe beam, E (in addition to the MOT beams). Each of these beams is near resonance with the $5s\,^2S_{1/2} \rightarrow 5p\,^2P_{3/2}$ transition in ^{85}Rb at 780 nm and must be frequency stable and independently tunable. To accomplish this, we constructed a single master extended-cavity diode laser (ECDL), whose absolute frequency is locked to an atomic resonance, and three additional lasers injection-locked to the master. We use various frequency offset techniques to generate E_1, E_2, and E, as follows.

In Fig. 4, we show an overview of the injection locking scheme. The frequency Ω_0 of the master laser is locked to a saturated absorption crossover resonance in a Rb vapor cell. We derive the pump field, E_1, using the laser labeled E_1. A small portion of the master laser beam is directed into this high-power, bare laser diode, injection locking its frequency directly to Ω_0. This pump beam is frequency shifted by an amount $f_{\mathrm{AO}} \sim 200$ MHz in an acousto-optic modulator (AOM) before being directed into the MOT. Thus the frequency of this beam is $\Omega_1 = \Omega_0 - 2\pi f_{\mathrm{AO}}$. (We diagram the laser frequencies and atomic resonance frequencies in Fig. 5.)

The second pump field E_2 is derived from an ECDL that is frequency offset from the master laser by an amount $f_\mu \sim 3$ GHz using a microwave offset locking technique. This beam is also frequency offset in the same AOM described above by f_{AO} before entering the MOT. We tune the frequency f_μ to equal the hyperfine splitting of the ground state of ^{85}Rb, less the detuning of the pump field from two-photon resonance, resulting in a pump beam frequency of $\Omega_2 = \Omega_0 - 2\pi f_{\mathrm{AO}} + |\omega_{21}| + \tilde{\delta}$. In the microwave offset locking technique, we modulate the diode laser injection current with a signal at the microwave frequency f_μ to produce small sidebands on the optical field [24]. Optical injection locking occurs when one of the diode laser modulation sidebands is tuned within the capture range of the injected frequency Ω_0. We derive an error signal from the interference between the master laser and the diode laser, which we use to stabilize the laser. (In brief, we combine this diode laser output and the master laser output on a fast photodiode and observe the beat signal at frequency f_μ. The phase of this rf signal varies across the capture range. By mixing this beat signal with the output of the f_μ oscillator in a double-balanced mixer, we generate a dc error signal related to this phase, which enables long-term stabilization of the diode laser frequency. High-performance phase locking as described here is detailed in Ref. [25].)

Finally, we describe the generation of the probe field E, whose frequency must be independently tunable across Ω_1 (e.g., positive, negative, and zero frequency offsets). We accomplish this using a second offset injection locking technique, an electro-optic modulator (EOM), and an AOM. In this case, we place modulation sidebands on a beam picked off from the master laser output with an EOM driven at a frequency f_{EO}, and we inject this modulated laser into another ECDL, which is used to derive the probe field, E. Similar to the E_2 laser case, we observe injection locking when the probe laser is tuned within a capture range of the master laser carrier or one of its sidebands. In this case, we observe a dc interference signal between the master and probe laser, which is suitable for locking without the need for demodulation.

Again, using this technique we are able to maintain stable injection locking for many hours. To place the frequency of this beam in the required range, we double-pass it through an AOM, driven at frequency $f_{AO'} \sim 200$ MHz, to apply a second frequency offset, after which the frequency of the probe beam is $\Omega = \Omega_0 + 2\pi(f_{EO} - 2f_{AO'})$. This method produces a wide range of frequency offsets between the probe E and the pump E_1 fields. The frequency offset can be made quite small, as long as the capture ranges of the master laser carrier and sidebands do not interfere with one another. The upper limit of the frequency offset appears to be limited only by rf components used for frequencies up to the single-mode tuning range of the probe laser ECDL. With our choice of components, we are readily able to generate EO sidebands in the range of about 100–500 MHz, which is much greater than required for the experiments presented here. When $2f_{AO'} - f_{EO} = f_{AO}$, the probe laser frequency, Ω, is equal to the pump laser frequency, Ω_1. The frequency detuning between the probe and master laser can then be tuned by changing the value of f_{EO}. As a practical matter, this seemingly complicated scheme allows us to explore the NLPP process over a wide range of detunings by changing rf synthesizer frequencies, with a minimal realignment of optical beams.

In the present experiment, we are interested in measuring small changes in the transmission of the probe beam through the MOT in the presence of off-resonant, but intense, pump beams. We choose to leave the probe beam on constantly during the experiment, at an intensity low enough so as not to disrupt the MOT measurably. We are, however, required to switch off the pump beams during the MOT loading cycles. To this end we use the pump AOM described above as an optical shutter, with turn-on and turn-off times of several tens of nanoseconds, which is faster than the time scales important to the NLPP experiment. We direct the collinear pump beams through the center of the MOT. The probe is also directed through the center of the MOT, but at a small angle with respect to the pump beams to allow us to separate the beams and measure the power of the probe beam after the MOT.

In order to minimize the pump beam intensity variation across the probe beam, we chose to use pump beams (2–4-mm diameter) that are significantly larger than the probe beam (∼0.5-mm diameter). With this constraint and our low-power laser diodes, we are able to produce intensities of about 500 mW/cm^2 in each of the pump beams. We also keep the probe intensity as low as possible, typically on the order of 10 mW/cm^2, while maintaining good signal-to-noise ratio with our fast photodiode.

We perform the probe absorption measurements by cycling the MOT in periods of trapping and measurement, and we record the transmission of the probe beam for an interval of time before and after the pump beams are turned on. We cycle the entire experiment at about 10–20 Hz, which allows fast data acquisition while maintaining a trapping cycle that is long enough to recapture atoms lost during the expansion of the cold atoms after the trap is turned off and those lost during the probe cycle. The experimental cycle begins with a trapping period, after which the magnetic field coils are turned off. After the magnetic field decreases sufficiently (several milliseconds) the trapping light is turned off, and a short time later (<1 ms) the repumping light is turned off. About 1 ms later, the measurement cycle is initiated by turning on the pump fields as described above. We keep the duration of the measurement cycle short (∼50 μs) to maximize the time the MOT is on and thereby maintain a high atom number in the trap.

We continuously monitor the probe power transmitted through the MOT, and we record its change when the pump beams are switched on. This provides a direct measurement of the modification of the probe absorption due to the action of the pump beams. We average the transient signals over several (∼10) MOT cycles, which significantly improves the signal-to-noise ratio. This method allows us to examine the different time-dependent processes at play and their relative time scales. After each series of averages, the probe beam detuning δ_1 is stepped and the process repeated until a full spectrum is recorded. Using this method of detecting the probe absorption, we are able to observe how the system behaves in transient and steady-state regimes.

IV. RESULTS AND DISCUSSION

In this section we present the results of our measurements. We first present a variety of transient waveforms that illustrate the characteristic features we see in the data. We then present a series of spectra constructed from these transient waveforms to illustrate how the NLPP spectra change with two-photon detuning. Third, we present a series of probe absorption spectra in which we vary the intensity of the pump field, E_1, for a fixed intensity for pump field E_2. This series nicely illustrates that the probe absorption spectrum evolves from a two-photon absorption process to a Raman gain process as the intensity I_1 is increased. Finally, we discuss the role of optical pumping due to the small, but finite, population of the excited-state Rb atoms during the NLPP process and how this complicates a quantitative comparison of our results to the theoretical results of Berman and Dubetsky.

A. Transient waveforms

We show an example of the transient waveform in Fig. 6. In this figure, $t = 0$ μs indicates the time at which the pump beams turn on. The signal level before this time represents

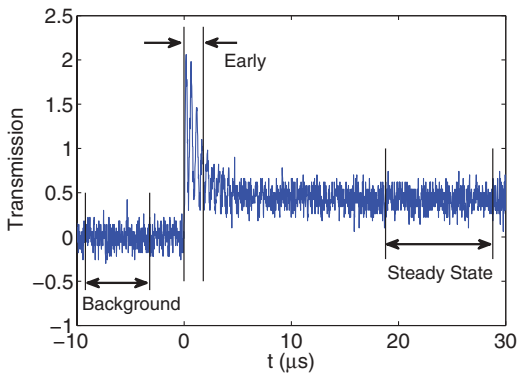

FIG. 6. (Color online) Representative probe transmission signal to illustrate data collection technique, in which the dc value of the probe transmission (labeled as Background) has already been subtracted. Time $t = 0$ represents the time that the pump beams are turned on. Early and steady-state signals are computed from averages over the time periods labeled Early and Steady State, respectively.

the background level, against which gain or absorption can be observed. Positive signals represent gain, while negative signals represent absorption. As seen in Fig. 6, the probe power undergoes a rapid change upon application of the pump beams. In this case, probe gain develops on a submicrosecond scale and then relaxes to a steady-state value, while undergoing damped oscillation at a frequency equal to the pump-probe detuning, δ_1. We designate the signal averaged over the first 1.5 μs after the pump fields are turned on as the "early" signal, and the signal after a 20-μs delay as the "steady-state" signal. We chose 1.5 μs as the duration for the early signal by considering two relevant time scales of the signal: 1.5 μs is long in comparison to the oscillation period (due to two-photon Rabi oscillation or pump-probe detuning), so our signal is an average over these oscillations. At the other bound, 1.5 μs is shorter than the relaxation time as the signal approaches steady state. The maximum gain that we observed was on the order of 1%.

The nature of the transient waveforms varies quite dramatically depending on the intensities of the pump beams and the pump and probe frequencies. We observe signatures within the transient waveforms at two different characteristic frequencies: the two-photon Rabi frequency, g, and the pump-probe detuning, δ_1. In Figs. 7–10 we show transient waveforms that are representative of the variety of NLPP signals we have observed. For each, the pump E_1 detuning and pump intensities are $\Delta_1/2\pi = -158$ MHz, $I_1 = 385$ mW/cm^2, and $I_2 = 232$ mW/cm^2. (In this and in the following examples, we specify only $\Delta_1^{(F=2)}$, which we abbreviate as Δ_1. This notation sufficiently identifies the laser frequency. The two relevant detunings are related by $(\Delta_1^{(F=2)} - \Delta_1^{(F=3)})/2\pi = 63$ MHz, the frequency difference between the $F = 3$ and $F = 2$ hyperfine states of the $5p\,^2P_{3/2}$ state.) For these intensities and detuning, the two-photon Rabi frequency $g/2\pi$ is 1.43 MHz for atoms starting from the $F = 3$, $|m_F| = 3$ level, and 1.05 MHz for atoms starting from the $F = 3$, $|m_F| = 2$ level. The average Stark shift is $S_1 - S_2 = 0.0$ MHz. We show

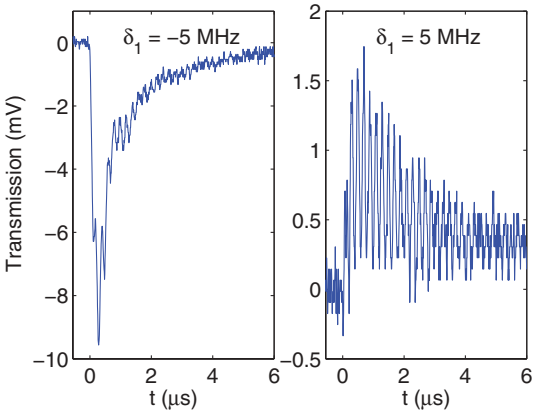

FIG. 7. (Color online) Transient NLPP signals for $\tilde{\delta} = -5$ MHz, $\delta_1/2\pi = \pm 5$ MHz. The waveform for $\delta_1/2\pi = -5$ MHz (left) shows a strong transient absorption with small oscillations at 5 MHz, while the waveform for $\delta_1/2\pi = +5$ MHz (right) shows oscillations of a similar amplitude at a frequency of 5 MHz on top of a smaller transient gain. The transients in this case decay to a small steady-state value with the same sign (absorption and gain) as the transients.

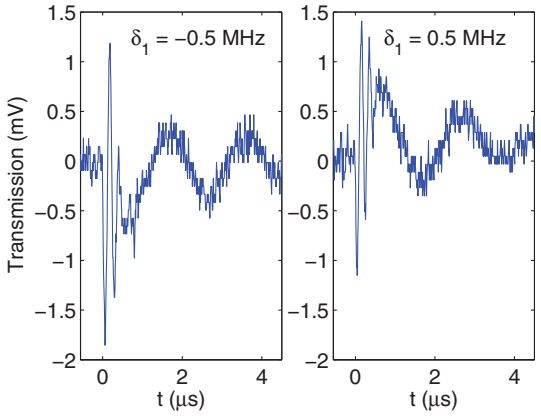

FIG. 8. (Color online) Transient NLPP signals for $\tilde{\delta}/2\pi = -5$ MHz, $\delta_1/2\pi = \pm 0.5$ MHz, near the central dispersion feature. The signal shows a short transient burst at the two-photon Rabi frequency, $g/2\pi = 4.4$ MHz, and a longer period oscillation at the pump-probe detuning, δ_1. The oscillations at frequency δ_1 show a π phase shift between $\delta_1/2\pi = \pm 0.5$ MHz, while the burst at the two-photon Rabi frequency has the same phase.

only a few microseconds of the full record length. Similar to the waveform shown in Fig. 6, each ultimately settles to a steady-state level. With the exception of Fig. 8, these waveforms show the transients at the peak of the absorption and gain features at a given two-photon detuning.

Figure 7 shows transients for $\tilde{\delta}/2\pi = -5$ MHz, which for $\delta_1/2\pi = -5$ MHz (left panel) show a strong early absorption with small-amplitude oscillations at a frequency of 5 MHz. The waveform for $\delta_1/2\pi = +5$ MHz (right panel) shows oscillations of a similar amplitude at a frequency of 5 MHz, imposed on top of a smaller early gain. The transients in this case decay to a very small steady-state value with the same sign (absorption or gain) as the early signal.

In Fig. 8, we show transients at a smaller pump-probe detuning δ_1, i.e., closer to the central dispersion feature, for $\tilde{\delta}/2\pi = -5$ MHz. These waveforms show a very pronounced

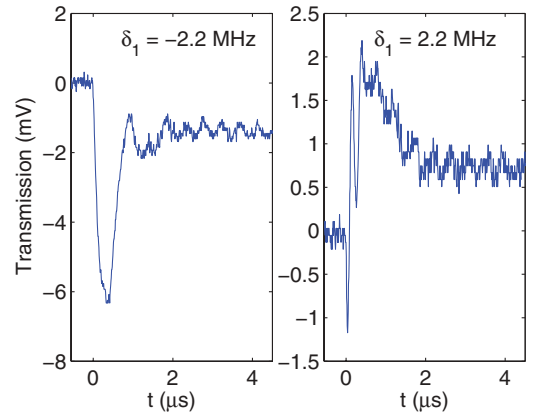

FIG. 9. (Color online) Transient NLPP signals for $\tilde{\delta}/2\pi = -1$ MHz, $\delta_1/2\pi = \pm 2.2$ MHz. In each of these transients, the transient and steady-state signals have the same sign, and the oscillations at frequency δ_1 are small. Interestingly, a short oscillating burst is visible at the beginning of the transient for $\delta_1/2\pi = +2.2$ MHz, while not for $\delta_1/2\pi = -2.2$ MHz.

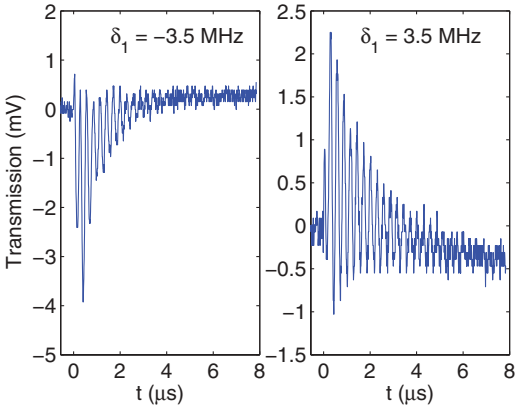

FIG. 10. (Color online) Transient NLPP signals for $\tilde{\delta}/2\pi = +3$ MHz, $\delta_1 = \pm 3.5$ MHz. The transients for $\delta_1 = \pm 3.5$ MHz have similar character. In each case, the steady-state and transient signals are opposite sign; e.g., steady-state absorption for $\delta_1 = -3.5$ MHz evolves to a small steady-state gain.

slow oscillation at frequency $\delta_1/2\pi = \pm 0.5$ MHz. In addition, they show a transient "burst" at a higher frequency, which lasts only for ~ 1 μs. This burst is present for all probe detunings, although it is often obscured when the transient signals vary with a similar frequency. However, close to $\delta_1 = 0$ the burst is clearly distinguishable from other signal components. The frequency of this burst, which we determine through computation of the Fourier transform of the time-dependent data, is the same for all values of δ_1, but varies with the two-photon detuning, $\tilde{\delta}$, as shown in Fig. 11. This variation suggests that this burst oscillation is related to two-photon Rabi cycling in the ground-state populations and manifested in the oscillation of the probe beam absorption signal. We fit the data in Fig. 11 to Eq. (7), using the two-photon Rabi frequency g and the differential Stark shift $S_1 - S_2$ as fitting parameters. The best-fit value of $g/2\pi$ is 1.26 MHz, and for $(S_1 - S_2)/2\pi$ is -1.19 MHz. While the Stark shift $S_1 - S_2$ does not agree

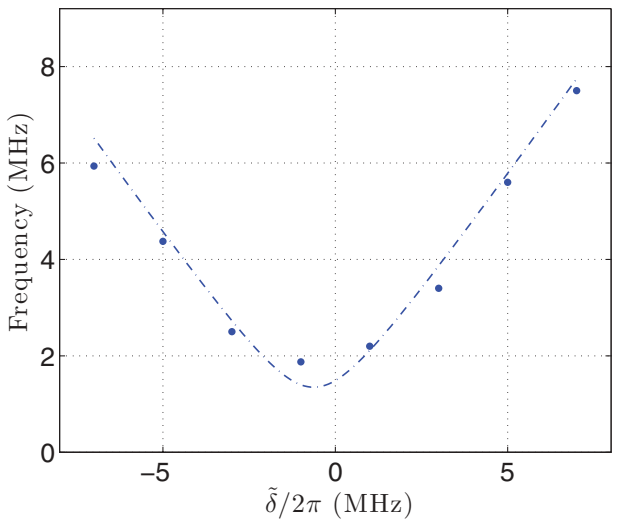

FIG. 11. (Color online) Experimentally measured burst transient frequencies (data points) and theoretical fit (dot-dashed blue line). We find the best-fit parameters are $g/2\pi = 1.26$ MHz and $(S_1 - S_2)/2\pi = -1.19$ MHz.

particularly well with the average value of 0.0 MHz that we calculated based upon the experimental parameters of I_1, I_2, and Δ, the value of $g/2\pi$ falls between the corresponding values that we calculated for the $|m_F| = 3$ and $|m_F| = 2$ states that we discussed earlier, which could be an indication that the population of atoms is preferentially distributed in states with larger m_F after the MOT is switched off. We note that this frequency displays a small negative chirp, shifting from high to low frequency.

In Fig. 9, we show a set of transients with much larger steady-state values, for a two-photon detuning $\tilde{\delta}/2\pi = -1$ MHz. In each case, the steady-state signal is the same sign as the early signal, and weak modulation at δ_1 is observed. Interestingly, there is a short burst oscillation at the two-photon Rabi frequency visible for $\delta_1/2\pi = +2.2$ MHz. This feature is not evident for $\delta_1/2\pi = -2.2$ MHz, but in the presence of the large, broad, negative initial peak for these data, it is unclear if this burst is absent in this case or simply obscured.

Finally, in Fig. 10 we show an example where the steady-state signal has the opposite sign from the early signal. Interestingly, the transients for $\delta_1/2\pi = \pm 3.5$ MHz have similar character, each having similar amplitude oscillations and steady-state value. We attribute the reversal of early gain to steady-state absorption (and vice versa) to optical pumping effects, as we discuss in Sec. IV E.

B. Varying pump detuning, $\tilde{\delta}$

We use the waveforms discussed in the previous section to generate a series of NLPP gain spectra, each as a function of the pump-probe detuning δ_1. In Figs. 12–15 we show the

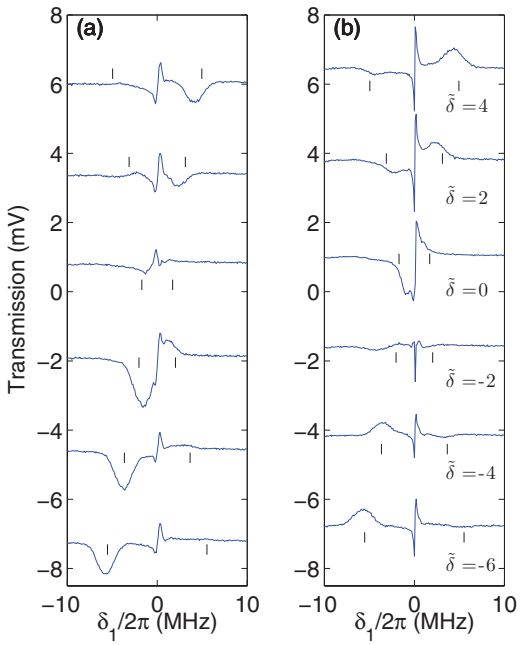

FIG. 12. (Color online) NLPP spectra for $\Delta_1/2\pi = -108$ MHz, $I_1 = 212$ mW/cm^2, and $I_2 = 62$ mW/cm^2: (a) transient signal spectra, (b) steady-state spectra. We vary $\tilde{\delta}$, as labeled on each curve in (b), for each of these spectra. The tick marks on each plot indicate $\delta_1 = \pm\omega_{BA}$, computed using Eq. (7), with $g = g^{(|m_F|=3)}$ as listed in Table I.

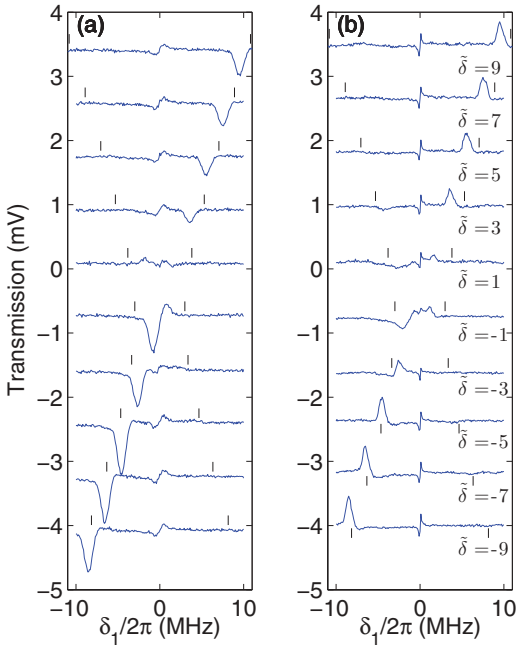

FIG. 13. (Color online) NLPP spectra for $\Delta_1/2\pi = -108$ MHz, $I_1 = 398$ mW/cm^2, and $I_2 = 119$ mW/cm^2: (a) transient signal spectra, (b) steady-state spectra. We vary $\tilde{\delta}$, as labeled on each curve in (b), for each of these spectra. The tick marks on each plot indicate $\delta_1 = \pm\omega_{BA}$, computed using Eq. (7), with $g = g^{(|m_F|=3)}$ as listed in Table I.

dependence of the NLPP spectra on the two-photon detuning $\tilde{\delta}$. The range of $\tilde{\delta}/2\pi$ for our measurements varies for the different data sets, with the maximum value of ± 10 MHz.

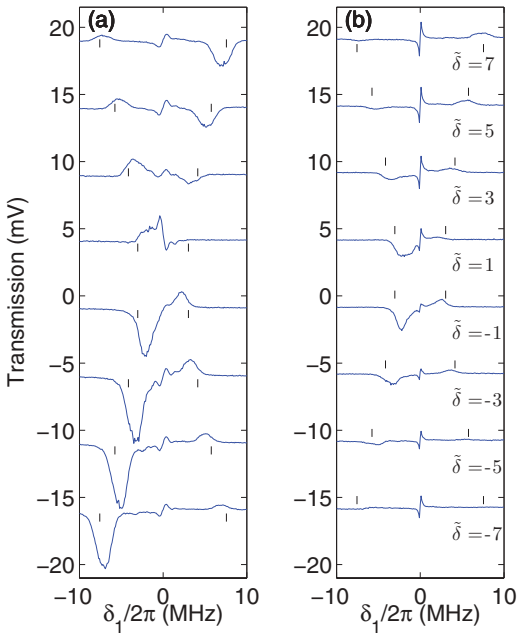

FIG. 14. (Color online) NLPP spectra for $\Delta_1/2\pi = -158$ MHz, $I_1 = 385$ mW/cm^2, and $I_2 = 232$ mW/cm^2: (a) transient signal spectra, (b) steady-state spectra. We vary $\tilde{\delta}$, as labeled on each curve in (b), for each of these spectra. The tick marks on each plot indicate $\delta_1 = \pm\omega_{BA}$, computed using Eq. (7), with $g = g^{(|m_F|=3)}$ as listed in Table I.

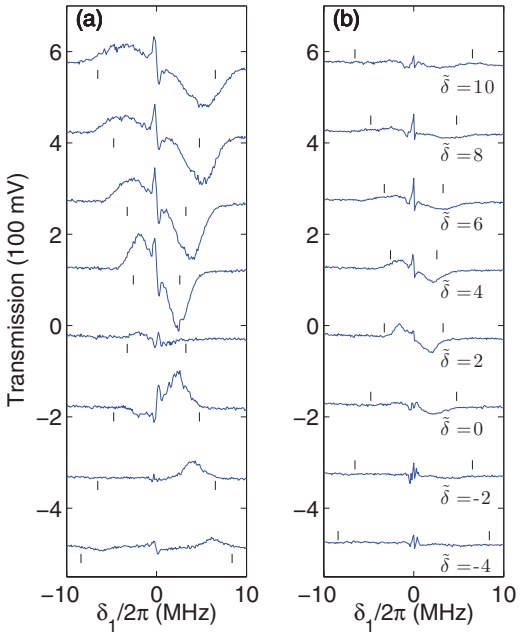

FIG. 15. (Color online) NLPP spectra for $\Delta_1/2\pi = +292$ MHz, $I_1 = 477$ mW/cm^2, and $I_2 = 356$ mW/cm^2: (a) transient signal spectra, (b) steady-state spectra. We vary $\tilde{\delta}$, as labeled on each curve in (b), for each of these spectra. The tick marks on each plot indicate $\delta_1 = \pm\omega_{BA}$, computed using Eq. (7), with $g = g^{(|m_F|=3)}$ as listed in Table I.

Since the waveforms display rather different behaviors, there are several parameters needed to fully quantify them. The spectra that we determine display two of these parameters: the early response and the steady-state response. Each of these is indicated in the transient waveform shown in Fig. 6. As we stated earlier, we define the early response as the average of the transient waveform over the first 1.5 μs after the pump lasers are turned on, and the steady-state response as the average signal strength after the transient behavior of the waveform has died away. The NLPP spectra consist of, in general, three features: rather broad absorption or gain peaks near $\delta_1 = \pm\omega_{BA}$, where $\omega_{BA} = \sqrt{\delta^2 + 4g^2}$, and a strong (usually dispersion-shaped) feature near $\delta_1 = 0$. We have marked $\pm\omega_{BA}$ on each plot with short tick marks to aid the eye. For this purpose, we use $g^{(|m_F|=3)}$, as defined in Eq. (8), to calculate ω_{BA}. We understand the peak near $\delta_1 = \tilde{\delta}$ as the direct two-photon Raman transition of the atom with the probe beam and E_2. We see absorption or gain at this peak depending, as we support later, on the relative populations of states $|1\rangle$ and $|2\rangle$. We estimate the uncertainty of the data points of these spectra to be about 10 μV for Figs. 12–14, or slightly greater than the width of the lines. For Figs. 15 and 16, the data were collected with a different detector and the uncertainty is about 0.5 mV, but the signal-to-noise ratio is similar.

We present a summary of the experimental parameters for each of the series of experiments performed in Table I. We list the field detuning, intensities, the two-photon Rabi frequency, g, and Stark shifts $S_1 - S_2$ that are important to the spectra shown in this section. We display the field detuning Δ_1 with two values: the first value is the detuning from the $F = 2$ excited state, and the second from the $F = 3$ excited state. The

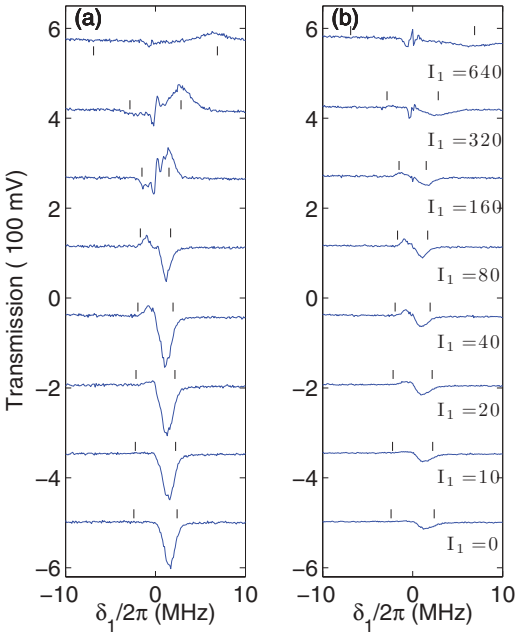

FIG. 16. (Color online) NLPP spectra for $\Delta_1/2\pi = +292$ MHz, $\tilde{\delta} = 0$, and $I_2 = 356\,\mathrm{mW/cm^2}$: (a) transient signal spectra, (b) steady-state spectra. The intensity I_1 varies, taking values of 0, 10, 20, 40, 80, 160, 320, and 640 $\mathrm{mW/cm^2}$. The tick marks on each plot indicate $\delta_1 = \pm\omega_{BA}$, computed using Eq. (7), with $g = g^{(|m_F|=3)}$ as listed in Table I.

two-photon Rabi frequencies $|g|$ and differential Stark shift $S_1 - S_2$ are as we described in Sec. III. The two values of the Rabi frequency $|g|$ represent $|g^{(|m_F|=3)}|/2\pi$ and $|g^{(|m_F|=2)}|/2\pi$, i.e., the interaction strength when the initial state of the $F = 3$ ground-state atoms is $|m_F| = 3$ and $|m_F| = 2$, respectively.

We show the lowest-intensity data in Fig. 12, where we have set $\Delta_1/2\pi = -108$ MHz, $I_1 = 212\,\mathrm{mW/cm^2}$, and $I_2 = 62\,\mathrm{mW/cm^2}$. For the spectra for which $|\tilde{\delta}/2\pi| > 2$ MHz, there is little evidence of any peak at $\delta_1 = -\tilde{\delta}$. The peak near $\delta_1 = \tilde{\delta}$ shows absorption in the early spectrum, but gain in the steady-state spectrum. The dispersion-shaped feature at $\delta_1 = 0$ is, in each case, of the same polarity: negative for δ_1 slightly less than 0, and positive for δ_1 slightly greater than 0. We label this the positive polarity, and the inverted shape the negative polarity.

In Fig. 13, $\Delta_1/2\pi = -108$ MHz remains the same, but we have increased I_1 to 398 $\mathrm{mW/cm^2}$ and I_2 to 119 $\mathrm{mW/cm^2}$. The probe intensity is $\lesssim$10 $\mathrm{mW/cm^2}$. These spectra are qualitatively similar to those in Fig. 12, with the transient spectra showing strong absorption at $\delta_1 = \tilde{\delta}$, and gain peaks at these δ_1 in the steady-state spectra. The dispersion-shaped feature at $\delta_1 = 0$ is also similar, showing constant polarity in each case as well. Perhaps the most notable feature of these two series of data is that the linewidth is sub-megahertz throughout.

We start to see some variation in the spectra of Fig. 14, for which we have increased the intensity I_2 to 232 $\mathrm{mW/cm^2}$, but kept $I_1 = 385\,\mathrm{mW/cm^2}$ similar to the previous value. We have also increased $\Delta_1/2\pi$ to -158 MHz. The probe beam intensity is 42 $\mathrm{mW/cm^2}$. While the absorption peak in the early spectrum near $\delta_1 = \tilde{\delta}$ is still the strongest feature, the peak near $\delta_1 = -\tilde{\delta}$ is now evident, and shows gain for all $\tilde{\delta}$. Perhaps even more interesting is the sign of the corresponding peaks in the steady-state spectra. The peak at $\delta_1 = \tilde{\delta}$, which showed gain in the lower-intensity spectra of Figs. 12 and 13, now shows absorption for $\tilde{\delta} < 0$, but gain for $\tilde{\delta} > 0$. With one exception, the polarity of the dispersion-shaped feature at $\delta_1 = 0$ is the same as it was in the low-intensity spectra, but very weak in the early spectra. The notable exception to this observation can be seen in the early spectrum, for $\tilde{\delta} = +1$, in which the polarity of this central feature is inverted.

We have recorded the additional NLPP spectra with these same intensities, but for which $\Delta_1/2\pi$ to -108 MHz, which we do not show. These spectra are very similar to those shown in Fig. 14.

For our final data set showing the variation of the NLPP spectra vs $\tilde{\delta}$, we have tuned the pump lasers to $\Delta_1 > 0$, i.e., frequencies greater than the single-photon transition

TABLE I. The parameters relevant to the NLPP spectra shown in Figs. 12–16. The two values for the detuning Δ_1 are $\Delta_1^{(F=2)}$, the detuning from the $F = 2$ excited state, and $\Delta_1^{(F=3)}$, the detuning from the $F = 3$ excited state. The two-photon Rabi frequencies $|g|$ are $|g|^{(|m_F|=3)}$, for atoms initially in the $|m_F| = 3$ component of the $F = 3$ ground state, and $|g|^{(|m_F|=2)}$, for atoms initially in the $|m_F| = 2$ component, as computed using Eqs. (8) and (9). The two-photon Stark shift $S_1 - S_2$ includes a sum of contributions for each ground-state magnetic sublevel from all excited states and does not vary significantly across ground-state magnetic sublevels.

Figure	$\Delta_1/2\pi$ (MHz)	I_1 ($\mathrm{mW/cm^2}$)	I_2 ($\mathrm{mW/cm^2}$)	$\lvert g\rvert/2\pi$ (MHz)	$S_1 - S_2$ (MHz)
12	−108/−171	212	62	0.78/0.55	−0.7
13	−108/−171	398	119	1.48/1.04	−1.4
14	−158/−221	385	232	1.43/1.05	0.0
15	292/229	477	356	1.29/1.14	4.0
		0		0/0	−2.4
		10		0.187/0.165	−2.2
		20		0.264/0.234	−2.1
16	292/229	40	356	0.373/0.331	−1.8
		80		0.529/0.468	−1.3
		160		0.748/0.662	−0.2
		320		1.057/0.936	1.9
		640		1.495/1.323	6.2

frequencies: $\Delta_1/2\pi = +292$ MHz. These spectra are shown in Fig. 15. The pump laser intensities are also greater, with $I_1 = 477$ mW/cm^2 and $I_2 = 356$ mW/cm^2, and the probe beam intensity is $\lesssim$10 mW/cm^2. The peaks in the transient spectra at $\delta_1 = \pm\tilde{\delta}$, while weak for $\tilde{\delta} < 0$, show the same signature as those in Fig. 14, i.e., absorption at $\delta_1 = \tilde{\delta}$ and gain at $\delta_1 = -\tilde{\delta}$ for all $\tilde{\delta}$. The dispersion-shaped feature at $\delta_1 = 0$, however, has reversed polarity. For $\tilde{\delta} < 0$ it has the same sign as the low-intensity data, but reverses for $\tilde{\delta} > 0$. The peaks in the steady-state spectra are reversed from those in Fig. 14: gain at $\delta_1 = \tilde{\delta}$ for $\tilde{\delta} < 0$ and absorption for $\tilde{\delta} > 0$, and absorption at $\delta_1 = -\tilde{\delta}$ for $\tilde{\delta} < 0$ and gain for $\tilde{\delta} > 0$. The dispersion-shaped feature at $\delta_1 = 0$ has reversed sign for $\tilde{\delta}/2\pi = 0$ and $\tilde{\delta}/2\pi = +4$ MHz.

C. Varying pump intensities

We show in Fig. 16 a series of probe transmission spectra for varying intensity I_1 of the pump E_1 field. The pump laser frequencies are tuned to the two-photon Raman resonance, $\tilde{\delta} = 0$, the single-photon detuning from the $F = 2$ state is $\Delta_1/2\pi = +292$ MHz, the intensity of pump E_2 is $I_2 = 356$ mW/cm^2, and the probe beam intensity is $\lesssim$10 mW/cm^2. We observe that the early spectra and the steady-state spectra are quite different from one another. For $I_1 = 0$ we see a simple absorption profile that is Stark-shifted toward higher frequencies due to E_2. As I_1 increases, we see the spectrum begin to change considerably. In the early spectrum, absorption turns to gain for $\delta_1 > 0$, with the frequency of the peak occurring near $\delta_1 = 2g$. The central peak at $\delta_1 = 0$ becomes dispersion-shaped with increasing I_1. The steady-state spectrum, on the other hand, shows an absorption peak near $\delta_1 = 2g$. These spectra are rather complicated for increasing I_1, showing rapid fluctuations near $\delta_1 = 0$ for $I_1 \geqslant 160$ mW/cm^{-2}.

D. Comparison of early spectra to theoretical steady state

While the steady-state spectra observed in the experiment share some features, under some conditions, with the steady-state theoretical spectra, broad agreement is lacking because the theory does not include optical pumping effects, nor does it include the many magnetic sublevels in the real atom. Before discussing these effects, we compare the early spectra recovered from the data with the steady-state theory. We focus our attention on the data shown in Fig. 14, where $\Delta_1/2\pi = -158$ MHz, $I_1 = 385$ mW/cm^2, $I_2 = 232$ mW/cm^2, as listed in Table I, and the probe beam intensity $I = 42$ mW/cm^2. We note that the Rabi frequencies and Stark shift parameters listed in Table I for a single three-level subsystem do not faithfully reproduce the experimental spectra. Our goal is to find a set of effective values for the two-photon Rabi frequency, g, the Stark shifts, S_1 and S_2, and the ratio of Rabi frequencies, η, that allow us to reproduce the early spectra shown in Fig. 14.

We measure the frequency detuning (δ_1) of the peaks of the absorption and gain resonances (which are symmetric about $\delta_1 = 0$) from Fig. 14(a) and plot these as a function of $\tilde{\delta}$ (green) in Fig. 17. We fit these detunings to Eq. (7) to determine the best-fit parameters (dotted green line), which yields $g/2\pi = 0.76$ MHz, and $(S_1 - S_2)/2\pi = 0$ MHz. We then use these parameters to obtain the theoretical spectra

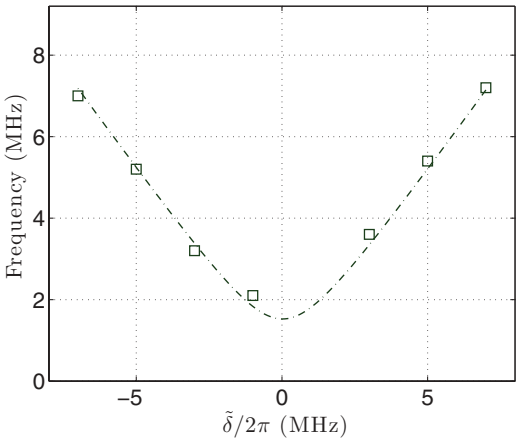

FIG. 17. (Color online) Experimentally measured absorption and gain resonant frequencies (green squares) and theoretical fit (dot-dashed green line) vs two-photon field detuning $\tilde{\delta}$ for the data shown in Fig. 14. We find the best-fit parameters are $g/2\pi = 0.76$ MHz and $(S_1 - S_2)/2\pi = 0$.

shown in blue (solid lines) in Fig. 18. We adjusted the value of η to best reproduce the relative heights of the gain and absorption peaks, and we find, for $\eta = 1.5$, the fit to be reasonable across all values of $\tilde{\delta}$. While the correspondence of this fit to the measured spectra is encouraging, it is important to recognize that the atom is not in steady state during this time, as the model of Ref. [22] assumes; the dispersion-shaped feature at $\delta_1 = 0$ of the experimental spectra is much more pronounced than that in the calculated spectra, the ratio η is not theoretically independent of g and $S_1 - S_2$, and the best-fit values do not make up a consistent set of simple three-level atomic parameters. All of these suggest that a more complete

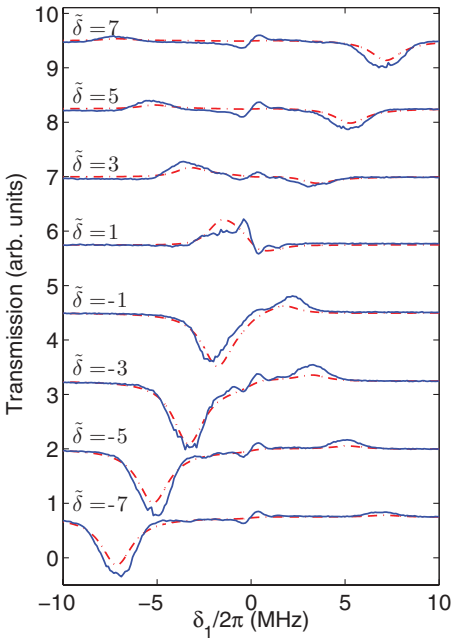

FIG. 18. (Color online) Theoretical steady-state NLPP spectra (dot-dashed red lines) for $\Delta_1/2\pi = -158$ MHz, $g/2\pi = 0.76$ MHz, $(S_1 - S_2) = 0$, and $\eta = 1.5$, plotted with the experimental early signal data (solid blue lines) from Fig. 14 for varying $\tilde{\delta}$.

model of the interaction is required for full understanding of these spectra.

E. Effect of population redistribution by the pump beams on steady-state spectra

The redistribution of the population of the various levels of the Rb atom plays a primary role in the steady-state spectra that we observe. In particular, the redistribution of the population qualitatively explains many of the differences between the transient and steady-state spectra, as well as the difference between either of these observed spectra and that predicted by Berman and Dubetsky. In Ref. [22], the authors considered the optical Bloch equations for the three-level system as described earlier. Since the pump lasers are far detuned from their respective single-photon transitions (i.e., Δ, Δ_1, and $\Delta_2 \gg \Gamma$), they adiabatically eliminated $|e\rangle$ from the equations and solved for the steady-state population difference,

$$W = \rho_{22}^{(0)} - \rho_{11}^{(0)} = \frac{(\Lambda_2 - \Lambda_1)}{\Gamma} \frac{\Gamma^2 + \delta^2}{\Gamma^2 + \delta^2 + 4|g|^2}, \qquad (10)$$

where damping of the system is due to departure of atoms from the interaction region. Λ_1 and Λ_2 in this expression are constants describing the incoherent growth rate of levels $|1\rangle$ and $|2\rangle$ due to some external agent. We show the line shape described by Eq. (10) as a function of two-photon detuning $\tilde{\delta}$ for different values of the Rabi frequency χ_2 in Fig. 19(a), using $\Lambda_1/2\pi = \Gamma/2\pi = 100$ kHz, and $\Lambda_2 = 0$. W approaches zero for larger values of χ_2 but never becomes positive. It always has the same sign as $(\Lambda_2 - \Lambda_1)$. The minimum of W occurs at the effective two-photon resonance, which is shifted relative to $\tilde{\delta} = 0$ by the ac Stark shift of levels $|1\rangle$ and $|2\rangle$ by the pump fields, E_1 and E_2. This measure of the population difference W differs in our laboratory measurements for several reasons. First, the initial population at the end of the trapping cycle in the MOT leaves the atoms primarily in level $|1\rangle$, the $5s\ ^2S_{1/2}, F = 3$, distributed among the various m_F substates. (We know very little of this initial distribution among the m_F states, in that the polarization of the trapping and repump fields, as well as the magnetic field of the MOT, vary throughout the trapping region.) During the measurement cycle, there is likely expansion of the atoms out of the interaction region, as well as collisions with background gas, that lead to damping of the system, but no mechanism that would lead to growth of the populations of levels $|1\rangle$ or $|2\rangle$, i.e., no appreciable values of Λ_1 or Λ_2. Second, the population of the excited state $|e\rangle$, and the subsequent spontaneous emission, cannot be ignored. While the pump fields E_1 and E_2, which drive the Rabi precession of the system at the rate g, are tuned well away from resonance with the single-photon transitions, there is a nonzero probability of excitation of state $|e\rangle$, which introduces damping to the system. We support this premise through study of the optical Bloch equations, which we analyze through numerical integration. We calculate the steady-state population difference in the bare state basis as $W = \rho_{22}^{(0)} - \rho_{11}^{(0)}$ using the density matrix formalism so that we may account for spontaneous emission from excited state $|e\rangle$. Using this formalism we can track the dependence of the population difference on the field parameters, in particular χ_2 and $\tilde{\delta}$. Solving the system of equations describing a three-level system coupled by the two intense pump fields, we obtain time-dependent solutions such as those shown in Fig. 20. There are a few notable features of these solutions. First, we notice that the population of the excited state, ρ_{ee}, is always small, but not zero; the spontaneous emission rate is proportional to this population. Second, we see that the ground-state populations have two primary contributions, an oscillating component and exponential decay. The oscillations occur at the two-photon Rabi frequency of the pump fields, and the exponential decay corresponds to the spontaneous emission scattering rate. We observe the greatest two-photon Rabi flopping amplitude when the two-photon resonance condition is met ($\delta = 0$),

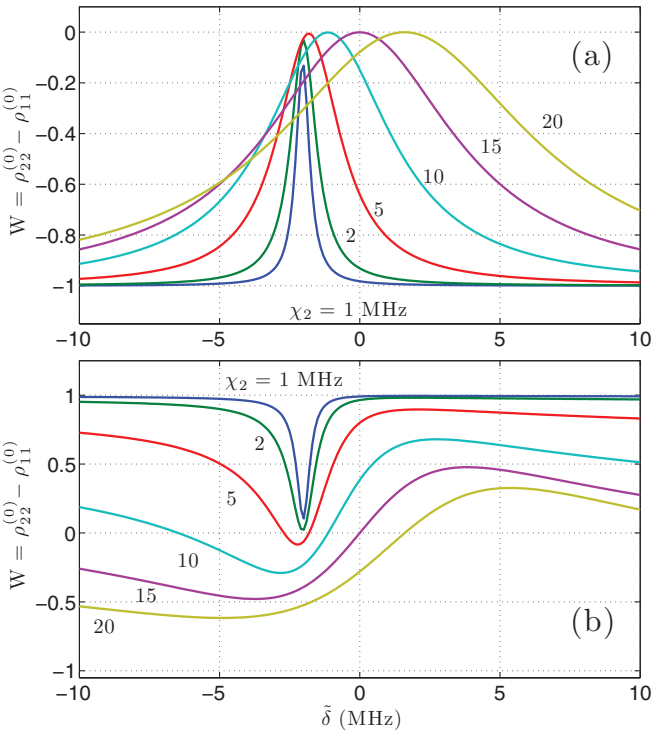

FIG. 19. (Color online) The population difference W from Ref. [22] (top), for $\Gamma/2\pi = 100$ kHz, and from numerical integration of the optical Bloch equations for the three-level system (bottom), for atoms initially in state $|1\rangle$ ($W = -1$). In each case the Rabi frequency $\chi_1/2\pi = 15$ MHz, and $\chi_2/2\pi$ is as labeled.

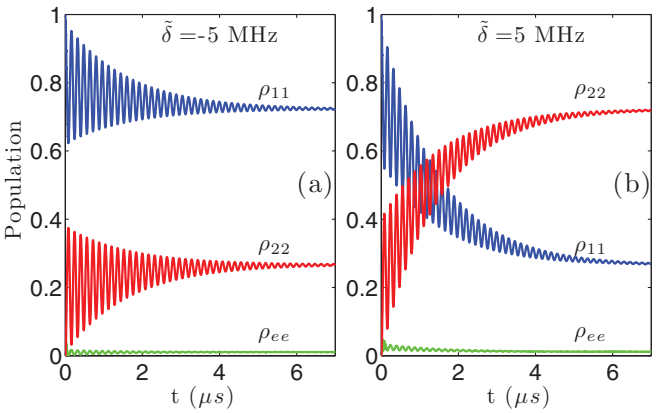

FIG. 20. (Color online) Time-dependent populations of states $|1\rangle$, $|2\rangle$, and $|e\rangle$, calculated by numerically integrating the optical Bloch equations: (a) $\tilde{\delta} = -5$ MHz, (b) $\tilde{\delta} = +5$ MHz.

in which case the steady-state population difference, W, is zero. For nonzero detunings a population difference develops, and in the case shown in Fig. 20 with Rabi frequencies $\chi_1/2\pi = \chi_2/2\pi = 15$ MHz, we see a population inversion that is equal and opposite for $\tilde{\delta}/2\pi = \pm 5$ MHz. Also, we note that the nature of the transient-state populations depends on the initial state, but the steady-state values do not. We compute the population difference for a range of detunings and numerically integrate the density matrix equations of motion to account for the effects of spontaneous emission. Although the population of the intermediate state is small compared to that of the ground states, spontaneous emission modifies the situation significantly.

We perform these calculations over a wide range of two-photon detunings and the Rabi frequency χ_2 for a particular value of χ_1. We show the dependence of the population difference W on χ_2 and $\tilde{\delta}$ in Fig. 19(b). In this simulation, $\chi_1/2\pi = 15$ MHz, and $\Delta_1/2\pi = -110$ MHz. This figure is very instructive as it clearly illustrates the intensity-dependent effects we see in our data. For small values of χ_2, in steady state, $W(t \to \infty) = 1$, which is a complete inversion from its initial value, $W(t = 0) = -1$, except near the two-photon resonance condition, where W approaches zero. The two-photon resonance is shifted to lower frequencies (for $\Delta < 0$) because of the ac Stark shift of $|1\rangle$ due to E_1.

As χ_2 is increased the line shape near the two-photon resonance broadens and becomes asymmetric. For $\chi_2/2\pi = \chi_1/2\pi = 15$ MHz we see that the steady-state value of W crosses zero at $\tilde{\delta} = 0$. For $\tilde{\delta} < 0$ we find $W < 0$, and for $\tilde{\delta} > 0$ we find $W > 0$. This impacts the probe absorption spectrum as follows: the population starts in state $|1\rangle$ ($W = -1$) and evolves as a damped sinusoid exponentially to the steady-state value of W. Therefore, we expect to see the transient and steady-state absorption and gain features to have the same sense for $\tilde{\delta} < 0$ and the opposite sense for $\tilde{\delta} > 0$. This is precisely what we observe in the data for red detunings from the intermediate states ($\Delta_1 < 0$).

V. CONCLUSION

In this work, we have presented measurements of the gain and absorption features of a weak probe laser beam interacting with a cooled sample of ^{85}Rb atoms strongly driven by a pair of pump fields via a Raman interaction coupling ground-state levels. We observe many of the features, including sideband peaks at the two-photon Rabi frequency and dispersion-shaped central peaks, predicted by the theory of Berman and Dubetsky in Ref. [22]. A more complete analysis, which includes the more complex structure of the atom and the damping of the interaction due to the weak off-resonant excitation of the $5p$ intermediate state, will be required for a full quantitative evaluation of the interaction.

ACKNOWLEDGMENTS

This material is based upon work supported in part by the US Army Research Office under Grant No. DAAD 19-03-1-0138. One of us (AKM) acknowledges support through the Graduate Assistance in Areas of National Need program of the Department of Education. We also acknowledge useful suggestions by and conversations with P. R. Berman, R. Yamazaki, and M. Gunawardena.

[1] See, for example, S. Dieter, *The Physics of Laser-Atom Interactions* (Cambridge University Press, Cambridge, 1997).
[2] F. Y. Wu, S. Ezekiel, M. Ducloy, and B. R. Mollow, Phys. Rev. Lett. **38**, 1077 (1977).
[3] R. W. Boyd and M. Sargent III, J. Opt. Soc. Am. B **5**, 99 (1988).
[4] G. Grynberg and C. Cohen-Tannoudji, Opt. Commun. **96**, 150 (1993).
[5] P. R. Berman, Phys. Rev. A **53**, 2627 (1996).
[6] P. R. Berman and G. Khitrova, Opt. Commun. **179**, 19 (2000).
[7] M. T. Gruneisen, K. R. MacDonald, and R. W. Boyd, J. Opt. Soc. Am. B **5**, 123 (1988).
[8] J. W. R. Tabosa, G. Chen, Z. Hu, R. B. Lee, and H. J. Kimble, Phys. Rev. Lett. **66**, 3245 (1991).
[9] M. Mitsunaga, T. Mukai, K. Watanabe, and T. Mukai, J. Opt. Soc. Am. B **13**, 2696 (1996).
[10] Y.-C. Chen, Y.-W. Chen, J.-J. Su, J.-Y. Huang, and I. A. Yu, Phys. Rev. A **63**, 043808 (2001).
[11] T. M. Brzozowski, M. Brzozowska, J. Zachorowski, M. Zawada, and W. Gawlik, Phys. Rev. A **71**, 013401 (2005).
[12] C. Monroe, D. M. Meekhof, B. E. King, and D. J. Wineland, Science **272**, 1131 (1996).
[13] L.-M. Duan, J. I. Cirac, P. Zoller, and E. S. Polzik, Phys. Rev. Lett. **85**, 5643 (2000).
[14] C. Genes and P. R. Berman, Phys. Rev. A **73**, 063828 (2006).
[15] A. D. Greentree, T. B. Smith, S. R. de Echaniz, A. V. Durrant, J. P. Marangos, D. M. Segal, and J. A. Vaccaro, Phys. Rev. A **65**, 053802 (2002).
[16] H. Li, V. A. Sautenkov, Y. V. Rostovtsev, G. R. Welch, P. R. Hemmer, and M. O. Scully, Phys. Rev. A **80**, 023820 (2009).
[17] V. I. Yudin, A. V. Taichenachev, Y. O. Dudin, V. L. Velichansky, A. S. Zibrov, and S. A. Zibrov, Phys. Rev. A **82**, 033807 (2010).
[18] D. F. Phillips, A. Fleischhauer, A. Mair, R. L. Walsworth, and M. D. Lukin, Phys. Rev. Lett. **86**, 783 (2001).
[19] A. V. Gorshkov, L. Jiang, M. Greiner, P. Zoller, and M. D. Lukin, Phys. Rev. Lett. **100**, 093005 (2008).
[20] H. Li, V. A. Sautenkov, M. M. Kash, A. V. Sokolov, G. R. Welch, Y. V. Rostovtsev, M. S. Zubairy, and M. O. Scully, Phys. Rev. A **78**, 013803 (2008).
[21] N. A. Proite, Z. J. Simmons, and D. D. Yavuz, Phys. Rev. A **83**, 041803 (2011).
[22] P. R. Berman and B. Dubetsky, Phys. Rev. A **62**, 053412 (2000).
[23] See, for example, D. Steck, http://steck.us/alkalidata/
[24] M. J. Snadden, R. B. M. Clarke, and E. Riis, Opt. Lett. **22**, 892 (1997).
[25] A. C. Bordonalli, C. Walton, and A. J. Seeds, J. Lightwave Technol. **17**, 328 (1999).